On steady rotational cyclonic flows: The viscous bidirectional vortex

Joseph Majdalani[1,a] and Martin J. Chiaverini[2]
[1]*University of Tennessee Space Institute, Tullahoma, Tennessee 37388, USA*
[2]*Orbital Technologies Corporation, Madison, Wisconsin 53717, USA*

(Received 10 October 2008; accepted 14 September 2009; published online 28 October 2009)

This study is focused on the tangential boundary layers of a bidirectional vortex, specifically those forming at the core and the sidewall of a swirl-driven cyclonic chamber. Our analysis is based on the regularized, tangential momentum equation which is rescaled in a manner to capture the forced vortex near the chamber axis and the no slip requirement at the sidewall. After identifying the coordinate transformations needed to resolve the rapid changes in the regions of nonuniformity, two inner expansions are constructed. These expansions are then matched with the outer, free vortex solution that is sandwiched between the core and the hard wall. By combining inner and outer expansions, uniformly valid approximations are subsequently obtained for the swirl velocity, vorticity, and pressure. These are shown to be strongly influenced by a dimensionless grouping that we refer to as the vortex Reynolds number, V. This keystone parameter appears as a ratio of the mean flow Reynolds number and the product of the swirl number and the chamber aspect ratio. Based on V, several fundamental features of the bidirectional vortex are quantified. Among them are the thicknesses of the viscous core and sidewall boundary layers; these decrease with $V^{1/2}$ and V, respectively. The converse may be said of the peak velocity which increases with $V^{1/2}$. In the same vein, the angular speed of the rigid-body rotation of the forced vortex is found to be linearly proportional to V. Our laminar swirl velocity is reminiscent of Sullivan's two-cell vortex except for its additional dependence on the aspect ratio of the chamber. For the purpose of verification, theoretical predictions are compared to particle image velocimetry measurements and Navier–Stokes simulations at high vortex Reynolds numbers. By properly accounting for the turbulent eddy viscosity in the analytical model, local agreement is obtained with both laboratory measurements and computer simulations. © *2009 American Institute of Physics*. [doi:10.1063/1.3247186]

I. INTRODUCTION

It has long been recognized that the free vortex assumption used to model the swirl velocity in columnar vortices deteriorates near the fluid's axis of rotation (e.g., Harvey[1] and Leibovich[2,3]). This is owed to the tangential velocity in a free vortex being inversely proportional to the distance measured from its center. Consequently, a free vortex overpredicts both the swirl velocity and the radial pressure gradients near its centerline. A similar feature has been reported by Long[4] in his classic study of the flow toward a rotating sink.

Although inviscid formulations can adequately describe the motion of unidirectional vortices, they can sometimes fail in capturing fundamental mechanisms associated with vortex instability. The remedy lies in rescaling the governing equations to the extent of incorporating the effects of viscosity, especially near the centerline. In this so-called "core" region, the rescaled equations reveal a forced vortex that exhibits the form suggested by Burgers,[5] Oseen,[6] Hamel,[7] or Schlichting.[8] Accordingly, the complete solution consists of, first, an outer free vortex and, second, an inner forced vortex undergoing solid-body rotation about its axis of revolution. The forced vortex behavior is strongly attributed to the presence of viscous shear stresses that intensify near the core. Due to the increasing shear that accompanies this dynamical motion, the swirl velocity vanishes at the chamber axis.

Bidirectional flows in cyclone separators and reverse vortex combustors exhibit analogous core vortex regions (see Lewellen[9]). The bipolar axial motion is further exacerbated by the presence of a thin Ekman layer at the headwall where the swirl velocity is brought to a stop.[9,10] However, endwall layers are often omitted in theoretical analyses due to their relative sizes and secondary influence on the bulk fluid motion.

Evidence of forced vortex behavior near the core of vortex chambers has been reported in several experimental and theoretical studies such as those by Kelsall,[11] Smith,[12,13] Reydon and Gauvin,[14] Vatistas *et al.*,[15] and Ogawa.[16] By combining experiments with numerical simulations, Hoekstra *et al.*[17] and, more recently, Hu *et al.*[18] independently confirmed the presence of a viscous core using laser-Doppler velocimetry (LDV) and computational fluid dynamics (CFD). Different simulation techniques have been employed including, to name a few, the Reynolds stress model (RSM) by Hu *et al.*,[18] Derksen and Van den Akker,[19] and Fang *et al.*,[20] the algebraic stress model by Boysan *et al.*,[21] and the arbitrary Lagrangian Eulerian (ALE) model by Murray *et al.*[22] Along similar lines, Rom *et al.*[23] collected valuable particle image velocimetry (PIV) measurements in bidirectional vortex chambers.

[a]Author to whom correspondence should be addressed. Mechanical, Aerospace and Biomedical Engineering Department, The University of Tennessee (UTSI), 411 B. H. Goethert Pkwy, MS-26, Tullahoma, TN 37388-9700. Telephone: (931) 393-7280. Electronic mail: maji@utsi.edu.

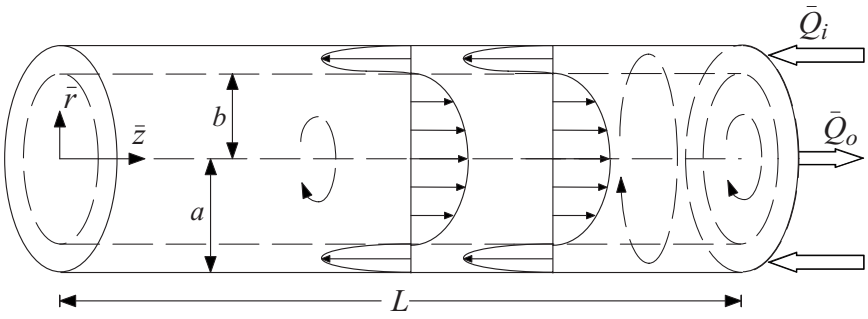

FIG. 1. Sketch of the bidirectional vortex chamber and corresponding coordinate system.

These independent studies have shown that the swirl velocity reaches a maximum at a small distance $\bar{\delta}_c$ from the chamber axis. This radial distance is viewed as a representative lengthscale of the core region surrounding the forced vortex. Furthermore, $\bar{\delta}_c$ is found to be nearly invariant along the chamber length. Being consistent with conventional boundary layer theory, $\bar{\delta}_c$ diminishes with successive increases in the Reynolds number. At the sidewall, a companion boundary layer $\bar{\delta}_w$ develops parallel to the core. As shown by Vatistas *et al.*,[24] the presence of $\bar{\delta}_c$ and $\bar{\delta}_w$ is characteristic of most vortex chambers including those driven by either unidirectional or bidirectional flow motion. Today, interest in vortex-driven combustors continues to be evidenced in developmental programs such as the vortex combustion cold-wall chamber by Chiaverini *et al.*,[25] the vortex fired hybrid engine by Gloyer *et al.*,[26] the vortex injection hybrid rocket engine by Knuth *et al.*,[27] and the reverse vortex combustor, also known as the tornado combustor by Matveev *et al.*[28]

Despite the abundance of numerical and experimental investigations of cylindrical cyclones, limited attention has been given to the advancement of viscous analytical models. This could be due to the overall complexity of the required equations in a fundamentally three-dimensional setting. Nonetheless, motivated by a propulsive application of cyclonic motion to an internal combustor, a theoretical investigation of the bidirectional flow field in a swirl-driven thrust chamber has recently given rise to a complex lamellar, inviscid solution.[29] This Euler formulation was extended to spherical geometry by Majdalani and Rienstra,[30] thereby uncovering additional families of solutions involving both linear and nonlinear vorticity-streamfunction representations. Majdalani[31] also derived several Eulerian mean flow profiles using the Bragg–Hawthorne equation as a starting point. These comprised helical motions of the Beltramian and Trkalian types with either linear or harmonic axial variations. Insofar as the thrust chamber resembled an inverted cyclone, the complex lamellar solution by Vyas and Majdalani[29] agreed favorably with existing experimental and numerical predictions of cyclonic flows when sufficiently removed from the core and sidewall regions.[29] It also agreed with existing empirical or semianalytical correlations that either neglected the axial dependence or relied on elemental regression fits. On the downside, this solution could neither satisfy the no slip condition at the wall nor account for the forced vortex structure that dominated the core. At the outset, its inviscid swirl velocity and radial pressure gradients became unbounded along the chamber axis.

The objective of this study is to improve the complex lamellar model of the bidirectional vortex by carrying out a dual point boundary layer analysis targeting the untreated core and sidewall regions. Our analysis starts by rescaling the momentum equation in the tangential direction. Being the undisputed source of singularity, this equation is regularized by retaining second-order viscous terms. Subsequently, the boundary layer equation is solved using the tools of matched asymptotic theory. In the process of matching, the free vortex expression is used to represent the outer expansion. Our approach leads to a uniformly valid approximation that exhibits the same distinctive features that are observed experimentally or acquired computationally. In light of the ensuing composite solution, the principal flow variables are examined and discussed. Experimental and numerical verifications are thus provided in addition to limiting process justifications.

II. MATHEMATICAL MODEL

Our geometry, nomenclature, and coordinate system are consistent with those employed by Vyas and Majdalani.[29] As shown symbolically in Fig. 1, the vortex chamber is modeled as a cylinder of radius a and length L. The headwall is closed while the aft section is attached to a tubular outlet of radius b. Using $\bar{r}$ and $\bar{z}$ to denote radial and axial coordinates, the outflow fraction of the radius at $\bar{z}=L$ is given by $\beta=b/a$, and the chamber's aspect ratio is taken as $l=L/a$. Everywhere, overbars are used to tag dimensional variables.

With the origin of the coordinate system being fixed at the center of the headwall, a single phase, incompressible, nonchemically reactive fluid enters the chamber at $\bar{z}=L$. It then spirals toward the headwall in the annular segment, $b<\bar{r}<a$, thus forming what is known as the "outer vortex." The spinning fluid reverses polarity at $\bar{z}=0$ due to radial attraction caused by the inward pressure gradient and low pressure region established near the centerline. After reversing direction, the returning flow is funneled axially out of the chamber through the inner segment, $0<\bar{r}<b$. This so-called "inner vortex" is separated from its outer counterpart by a spinning, nontranslating mantle along which the axial velocity vanishes identically. Our domain of interest extends over the interval $0\leq\bar{z}\leq L$ where several boundary conditions are prescribed. These are

$$\begin{cases} \bar{r}=a,\ \bar{z}=L,\ \bar{u}_\theta=U & \text{tangential velocity at entry,} \\ \bar{r}=a,\ \bar{z}<L,\ \bar{u}_\theta=0 & \text{no slip condition at the sidewall,} \\ \bar{r}=0,\ \forall\,\bar{z},\ \bar{u}_\theta=0 & \text{forced vortex center,} \\ \bar{z}=0,\ \forall\,\bar{r},\ \bar{u}_z=0 & \text{impervious headwall,} \\ \bar{r}=0,\ \forall\,\bar{z},\ \bar{u}_r=0 & \text{no flow across centerline,} \\ \bar{r}=a,\ \forall\,\bar{z},\ \bar{u}_r=0 & \text{impervious sidewall,} \\ 2\pi\displaystyle\int_b^a \bar{u}_z(\bar{r},L)\bar{r}d\bar{r}=\bar{Q}_i & \text{axial inflow matching tangential source.} \end{cases} \tag{1}$$

Note that $\bar{Q}_i$ represents the volumetric flow rate at the inlet. With A_i being the inlet injection area, $U\equiv\bar{u}_\theta(a,L)=\bar{Q}_i/A_i$ defines the average tangential injection speed at entry. To simplify the forthcoming analysis, all spatial coordinates and velocities are normalized by a and U, respectively. We consequently take

$$r=\frac{\bar{r}}{a},\quad z=\frac{\bar{z}}{a},\quad \delta=\frac{\bar{\delta}}{a},\quad u_r=\frac{\bar{u}_r}{U},\quad u_\theta=\frac{\bar{u}_\theta}{U},$$

$$u_z=\frac{\bar{u}_z}{U},\quad p=\frac{\bar{p}}{\rho U^2},\quad Q_i=\frac{\bar{Q}_i}{Ua^2}=\frac{A_i}{a^2},\quad \nabla=a\bar{\nabla}, \tag{2}$$

where δ represents a characteristic lengthscale. The normalized form of Eq. (1) becomes

$$\begin{cases} u_\theta(1,l)=1; & u_\theta(1,z<l)=0; & u_\theta(0,z)=0; & u_z(r,0)=0, \\ u_r(0,z)=0; & u_r(1,z)=0; & \displaystyle\int_\beta^1 u_z(r,l)rdr=\frac{Q_i}{2\pi}. \end{cases} \tag{3}$$

In reference to the complex-lamellar solutions of Vyas and Majdalani[29] or Majdalani and Rienstra,[30] the two additional boundary conditions that we seek to accommodate are the slip resistance at the wall, $u_\theta(1,z<l)=0$, and the swirl resistance at the core, $u_\theta(0,z)=0$. Since both requirements are a byproduct of viscous stresses, our starting point will be to regularize the tangential momentum equation following standard procedures (e.g., Balachandar *et al.*[32]). While the axial and radial equations may also be regularized, they are not considered here due to their secondary contributions and their decoupling from the tangential equations.

Given the underlying assumptions of axisymmetry and axial independence, u_θ does not affect the continuity equation. The axial and radial velocity components u_z and u_r remain related through

$$\frac{1}{r}\frac{\partial(ru_r)}{\partial r}+\frac{\partial u_z}{\partial z}=0\ \text{(continuity)}, \tag{4}$$

$$\frac{\partial(u_r\Omega_\theta)}{\partial r}+\frac{\partial(u_z\Omega_\theta)}{\partial z}=0\ \text{(vorticity transport)}, \tag{5}$$

and

$$\frac{\partial u_r}{\partial z}-\frac{\partial u_z}{\partial r}=\Omega_\theta\ \text{(vorticity)}, \tag{6}$$

with

$$\begin{cases} u_z(r,0)=0; & u_r(0,z)=0; \\ u_r(1,z)=0; & \displaystyle\int_\beta^1 u_z(r,l)rdr=\frac{Q_i}{2\pi}. \end{cases} \tag{7}$$

An exact solution for this set is given by[29]

$$\mathbf{u}=-\kappa\frac{\sin(\pi r^2)}{r}\mathbf{e}_r+u_\theta(r)\mathbf{e}_\theta+2\pi\kappa z\cos(\pi r^2)\mathbf{e}_z;$$

$$\kappa=\frac{1}{2\pi\sigma l}=\frac{A_i}{2\pi aL}, \tag{8}$$

where κ and σ represent the inflow parameter and modified swirl numbers, respectively. The latter is related to geometric constants via

$$\sigma=\frac{S}{\pi\beta}=\frac{a^2}{A_i}=\frac{1}{Q_i}. \tag{9}$$

Note that σ is a variant of the swirl number S, which is more commonly used in the literature (cf. Hoekstra *et al.*[17]).

In Eq. (8), the irrotational vortex $u_\theta=r^{-1}$ is obtained for a purely inviscid field.[29,30] It gives rise to a complex lamellar motion for which streamlines and isovorticity lines remain orthogonal everywhere by virtue of $\mathbf{u}\cdot\boldsymbol{\omega}=0$. Its main deficiencies are presented through its inclusion of a region of nonuniformity near $r=0$ and slippage at $r=1$. Note that the viscous treatment at the headwall, which mostly affects the swirl and radial velocities, will be excluded from the present analysis. As affirmed by Bloor and Ingham,[33] the singularity at $r=0$ is characteristic of most inviscid swirling flows to the extent of becoming archetypical. Therefore, in treating the core singularity and flow resistance at the sidewall, we revisit the θ-momentum equation and recognize that the deficit in the inviscid formulation is primarily due to the dismissal of second-order viscous terms. Their retention in the swirl momentum equation leads to

$$u_r\frac{\partial u_\theta}{\partial r}+\frac{u_r u_\theta}{r}=\frac{1}{\mathrm{Re}}\left(\nabla^2 u_\theta-\frac{u_\theta}{r^2}\right)$$
$$=\frac{1}{\mathrm{Re}}\frac{\partial}{\partial r}\left[\frac{1}{r}\frac{\partial(ru_\theta)}{\partial r}\right];\quad \mathrm{Re}\equiv\frac{Ua}{\nu},\tag{10}$$

where Re is the mean flow Reynolds number and ν is the kinematic viscosity. It should be noted that the axial independence of u_θ deteriorates near the headwall where a separate boundary layer treatment is required. In actuality, the assumption of axial invariance in the swirl velocity improves as l is increased. In cyclone separators and combustors, Re is of the order of 10^5. Recalling that $u_\theta=u_\theta(r)$ for $0<z<l$, $l\gg 1$, Eq. (10) reduces to an ordinary differential equation, specifically,

$$u_r\frac{du_\theta}{dr}+\frac{u_r u_\theta}{r}=\frac{u_r}{r}\frac{d}{dr}(ru_\theta)=\varepsilon\frac{d}{dr}\left[\frac{1}{r}\frac{d}{dr}(ru_\theta)\right];\quad \varepsilon\equiv\frac{1}{\mathrm{Re}}\ll 1.\tag{11}$$

For simplicity, we consolidate the angular momentum into one variable, $\xi\equiv ru_\theta$, and collapse Eq. (11) into

$$\varepsilon\frac{d}{dr}\left(\frac{1}{r}\frac{d\xi}{dr}\right)-\frac{u_r}{r}\frac{d\xi}{dr}=0.\tag{12}$$

Next, we convert the independent coordinate using

$$\eta\equiv\pi r^2.\tag{13}$$

This substitution transforms Eq. (12) into

$$\frac{\varepsilon}{\kappa}\frac{d^2\xi}{d\eta^2}+\frac{\sin\eta}{2\eta}\frac{d\xi}{d\eta}=0.\tag{14}$$

Given that $\kappa=(2\pi\sigma l)^{-1}\sim 10^{-2}-10^{-3}$, the size of κ causes the axial and radial velocities to remain much smaller than u_θ. At this juncture, we proceed by identifying the end point boundary layers that are responsible for the presence of forced vortex motion about the centerline and velocity adherence at the sidewall. Meanwhile, we note that the form of the outer solution may be recovered from Eq. (14) by suppressing viscosity. One is left with $d\xi^{(o)}/d\eta=0$, which is a statement of angular momentum conservation in a frictionless medium. Thus, using the superscript (o) to denote an outer approximation, we extract $\xi^{(o)}=\bar{C}$, where $\bar{C}$ is a constant.

III. TANGENTIAL CORRECTIONS

A. Inner, near-core approximation

In order to bring the swirl velocity to zero along the chamber axis, one must account for the rapid changes caused by the local emergence of viscous stresses (see Fig. 2). To do so, one may introduce the slowly varying scale,

$$s\equiv\frac{\eta}{\delta(\varepsilon)}.\tag{15}$$

This stretching transformation remaps the region of nonuniformity about the centerline to an interval of order unity. It also enables us to convert Eq. (14) into

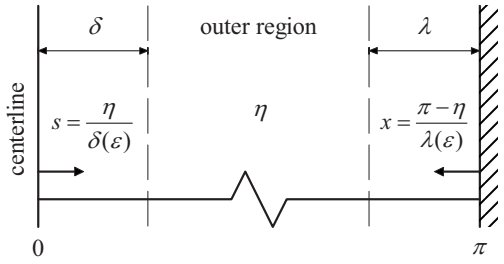

FIG. 2. Presence of dual end point boundary layers affecting the tangential velocity and causing it to vanish both at the centerline (thus giving rise to a forced vortex) and the sidewall (in observance of the no slip requirement).

$$\frac{\varepsilon}{\kappa\delta^2}\frac{d^2\xi}{ds^2}+\frac{\sin(\delta s)}{2\delta^2 s}\frac{d\xi}{ds}=0.\tag{16}$$

The resulting expression may be linearized near the core where $s\approx 0$. Straightforward expansion of the sine term in Eq. (16) yields

$$\frac{\varepsilon}{\kappa\delta}\frac{d^2\xi}{ds^2}+\frac{1}{2}\left[1-\frac{\delta^2 s^2}{3!}+O(\delta^2 s^2)\right]\frac{d\xi}{ds}=0.\tag{17}$$

Since both diffusive and convective terms strike a balance near the core, the two members of Eq. (17) appear at the same order when

$$\delta\sim\varepsilon/\kappa.\tag{18}$$

Having identified the distinguished limit for Eq. (17), one may take $\delta\equiv\varepsilon/\kappa=2\pi\varepsilon\sigma l$. Expressed in terms of the inner angular momentum variable, the core boundary layer equation becomes

$$\frac{d^2\xi^{(i)}}{ds^2}+\frac{1}{2}\frac{d\xi^{(i)}}{ds}=0,\tag{19}$$

where the superscript stands for the inner, near-core approximation. Using a series of the form $\xi^{(i)}=\xi_0^{(i)}+\delta\xi_1^{(i)}+\cdots$, one may determine successive viscous corrections to any desired order. Presently, a one-term inner solution of the form $\xi^{(i)}=\xi_0^{(i)}$ is sought. In the interest of simplicity, the subscript denoting the order in δ is discarded hereafter. The requirements that may be associated with Eq. (19) are those due to forced vortex motion and smooth transition to the outer solution, $\xi^{(o)}$. These conditions translate into

$$\begin{cases} r=0, & s=0, \quad \xi^{(i)}=0,\\ r\to 1, & s\to\infty, \quad \xi^{(i)}=\xi^{(o)}.\end{cases}\tag{20}$$

Forthwith, integration of Eq. (19) may be carried out with the outcome being

$$\xi^{(i)}=C_0\exp\left(-\tfrac{1}{2}s\right)+C_1.\tag{21}$$

As we insist on forced vortex behavior near the core, we set $\xi^{(i)}(0)=0$ and retrieve

$$\xi^{(i)}=C_0\left[\exp\left(-\tfrac{1}{2}s\right)-1\right].\tag{22}$$

The remaining constant C_0 may be obtained in harmony with the outer expansion. Using Prandtl's matching principle, we equate the outer limit of the inner solution to the inner limit of the irrotational vortex,

$$\lim_{s\to\infty} \xi^{(i)} = \lim_{\eta\to 0} \xi^{(o)}. \tag{23}$$

This process returns $C_0 = -\bar{C}$. A semiuniformly valid outcome is hence obtained that satisfies the forced vortex condition on one end of the domain but fails to secure the no slip requirement on the opposing end. This composite inner solution may be reconstructed from

$$\begin{aligned}\xi^{(ci)} &= \xi^{(i)} + \xi^{(o)} - [\xi^{(i)}]^{(o)} \\ &= \bar{C}\left[1 - \exp\left(-\tfrac{1}{2}\delta^{-1}\eta\right)\right] \\ &= \bar{C}\left[1 - \exp\left(-\tfrac{1}{2}\pi\kappa\varepsilon^{-1}r^2\right)\right] \\ &= \bar{C}\left[1 - \exp\left(-\tfrac{1}{4}Vr^2\right)\right],\end{aligned} \tag{24}$$

where V is the vortex Reynolds number obtained through the use of asymptotic theory. It is given by

$$V \equiv \frac{1}{\varepsilon\sigma l} = \frac{\mathrm{Re}}{\sigma}\frac{a}{L} = \frac{\rho U A_i}{\mu L} = \frac{\dot{m}_i}{\mu L}. \tag{25}$$

The injection mass flow rate appears as $\dot{m}_i$ while the density and viscosity of the fluid are given by ρ and μ. It is interesting to note the qualitative resemblance between Eq. (25) and the vortex Reynolds number encountered in two-cell swirling flows such as Sullivan's vortex;[34] Sullivan's control parameter is found to be proportional to the flow circulation at infinity and the reciprocal of the kinematic viscosity.

At this stage, the outer constant may be procured from the downstream condition of a tangentially injected fluid at entry. This implies

$$\xi^{(ci)}(1) = 1 \quad \text{or} \quad \bar{C} = \frac{1}{1 - \exp\left(-\tfrac{1}{4}V\right)} \simeq 1. \tag{26}$$

The composite inner solution becomes

$$\begin{cases} \xi^{(ci)} = \dfrac{1 - \exp\left(-\tfrac{1}{4}Vr^2\right)}{1 - \exp\left(-\tfrac{1}{4}V\right)} \simeq 1 - \exp\left(-\dfrac{1}{4}Vr^2\right), \\ u_\theta^{(ci)} = \dfrac{1}{r}\left[\dfrac{1 - \exp\left(-\tfrac{1}{4}Vr^2\right)}{1 - \exp\left(-\tfrac{1}{4}V\right)}\right] \simeq \dfrac{1}{r}\left[1 - \exp\left(-\dfrac{1}{4}Vr^2\right)\right]. \end{cases} \tag{27}$$

Note that as $\varepsilon \to 0$, $V \to \infty$, and $u_\theta^{(ci)} \to r^{-1}$, the swirl velocity associated with a free vortex is readily restored. Conversely, as $r \to 0$ at fixed ε, one can expand Eq. (27) into

$$u_\theta^{(ci)} = \frac{rV\left(1 - \tfrac{1}{8}Vr^2 + \tfrac{1}{96}V^2r^4 + \cdots\right)}{4\left[1 - \exp\left(-\tfrac{1}{4}V\right)\right]} = \frac{rV}{4} + O(r^3). \tag{28}$$

This expansion unravels the forced vortex relation, $u_\theta^{(ci)} \sim \omega_f r$, where

$$\omega_f = \tfrac{1}{4}V, \tag{29}$$

and ω_f represents the angular speed of the core layer which, due to the predominance of viscous stresses is induced to rotate as a solid rod around $r=0$.

B. Inner, sidewall approximation

In similar fashion, the sidewall boundary layer may be captured. Since $0 \le \eta \le \pi$, one rescales the thin region near the wall by setting

$$x \equiv \frac{\pi - \eta}{\lambda(\varepsilon)}, \tag{30}$$

where λ refers to the thickness of the wall tangential boundary layer. Using (w) to denote a sidewall solution, Eq. (14) may be rearranged into

$$\frac{\varepsilon}{\kappa\lambda^2}\frac{d^2\xi^{(w)}}{dx^2} - \frac{\sin(\pi - \lambda x)}{2\lambda(\pi - \lambda x)}\frac{d\xi^{(w)}}{dx} = 0. \tag{31}$$

Subsequently, Eq. (31) may be expanded in the vicinity of the wall to obtain

$$\frac{\varepsilon}{\kappa\lambda}\frac{d^2\xi^{(w)}}{dx^2} - \frac{1}{2}\left[1 - \frac{\pi^2}{6} + \frac{\pi\lambda x}{6} + O(\lambda^2x^2)\right]\frac{d\xi^{(w)}}{dx} = 0. \tag{32}$$

As before, a distinguished limit of $\lambda \equiv \varepsilon/\kappa$ ensures compatibility between diffusive and convective terms. At the outset, Eq. (32) becomes

$$\frac{d^2\xi^{(w)}}{dx^2} + \frac{1}{2}\left(\frac{1}{6}\pi^2 - 1\right)\frac{d\xi^{(w)}}{dx} = 0. \tag{33}$$

Corresponding boundary conditions consist of the no slip at the wall and the seamless blending of $\xi^{(w)}$ with the composite inner solution in the outer domain. Mathematically, one puts

$$\begin{cases} r = 1, \quad x = 0, \quad \xi^{(w)} = 0, \\ r \to 0, \quad x \to \infty, \quad \xi^{(w)} = \xi^{(ci)}. \end{cases} \tag{34}$$

Consequently, integration and satisfaction of the no slip at the sidewall lead to

$$\begin{aligned}\xi^{(w)} &= K_0\left\{\exp\left[-\tfrac{1}{2}\kappa\varepsilon^{-1}\pi\left(\tfrac{1}{6}\pi^2 - 1\right)(1 - r^2)\right] - 1\right\} \\ &= K_0\left\{\exp\left[-\tfrac{1}{4}\left(\tfrac{1}{6}\pi^2 - 1\right)V(1 - r^2)\right] - 1\right\}.\end{aligned} \tag{35}$$

This step is followed by matching with the composite outer solution, *viz.*,

$$\begin{aligned}&\lim_{r\to 0} \xi^{(w)} = \lim_{r\to 1} \xi^{(ci)} = 1 \quad \text{or} \\ &K_0 = \frac{1}{\exp\left[-\tfrac{1}{4}\left(\tfrac{1}{6}\pi^2 - 1\right)V\right] - 1} \simeq -1.\end{aligned} \tag{36}$$

The sidewall approximation becomes

$$\begin{cases} \xi^{(w)} = \dfrac{1-\exp\left[-\frac{1}{4}\left(\frac{1}{6}\pi^2-1\right)V(1-r^2)\right]}{1-\exp\left[-\frac{1}{4}\left(\frac{1}{6}\pi^2-1\right)V\right]} \simeq 1-\exp\left[-\dfrac{1}{4}\left(\dfrac{1}{6}\pi^2-1\right)V(1-r^2)\right], \\ u_\theta^{(w)} = \dfrac{1}{r}\left\{\dfrac{1-\exp\left[-\frac{1}{4}\left(\frac{1}{6}\pi^2-1\right)V(1-r^2)\right]}{1-\exp\left[-\frac{1}{4}\left(\frac{1}{6}\pi^2-1\right)V\right]}\right\} \simeq \dfrac{1}{r}\left\{1-\exp\left[-\dfrac{1}{4}\left(\dfrac{1}{6}\pi^2-1\right)V(1-r^2)\right]\right\}. \end{cases} \tag{37}$$

Evidently, the validity of Eq. (37) is restricted to a thin region above the wall. As we move toward the centerline, the outer solution is regained. Having explicitly identified the core and sidewall boundary layers, a unified approximation follows from the triple-merger of outer and inner expansions.

C. Composite, uniformly valid approximation

Using Erdélyi's idea of composite expansions,[35] a uniformly valid solution that extends over the range $0<z<l$ may be secured. This solution may be constructed by properly superimposing the end point boundary layers while subtracting their common limits. This consolidation process yields

$$\begin{aligned} \xi^{(c)} &= \xi^{(ci)} + \xi^{(w)} - [\xi^{(w)}]^{(o)} = \frac{1-\exp\left(-\frac{1}{4}Vr^2\right)}{1-\exp\left(-\frac{1}{4}V\right)} + \frac{1-\exp\left[-\frac{1}{4}\left(\frac{1}{6}\pi^2-1\right)V(1-r^2)\right]}{1-\exp\left[-\frac{1}{4}\left(\frac{1}{6}\pi^2-1\right)V\right]} - 1 \\ &\simeq 1-\exp\left(-\tfrac{1}{4}Vr^2\right) - \exp\left[-\tfrac{1}{4}\left(\tfrac{1}{6}\pi^2-1\right)V(1-r^2)\right]. \end{aligned} \tag{38}$$

The composite swirl velocity is thus at hand. Note that transcendentally small terms that often arise may be safely ignored due to the practical size of the vortex Reynolds number. Recognizing the open injection plane permitted at $z=l$, one can finally put

$$u_\theta = u_\theta^{(c)} = \begin{cases} \dfrac{1}{r}\left[\dfrac{1-\exp\left(-\frac{1}{4}Vr^2\right)}{1-\exp\left(-\frac{1}{4}V\right)} + \dfrac{1-\exp\left[-\frac{1}{4}\left(\frac{1}{6}\pi^2-1\right)V(1-r^2)\right]}{1-\exp\left[-\frac{1}{4}\left(\frac{1}{6}\pi^2-1\right)V\right]} - 1\right] \\ \qquad \simeq \dfrac{1}{r}\left\{1-\exp\left(-\dfrac{1}{4}Vr^2\right) - \exp\left[-\dfrac{1}{4}\left(\dfrac{1}{6}\pi^2-1\right)V(1-r^2)\right]\right\}; \quad 0<z<l, \\ \dfrac{1}{r}\left[\dfrac{1-\exp\left(-\frac{1}{4}Vr^2\right)}{1-\exp\left(-\frac{1}{4}V\right)}\right] \simeq \dfrac{1}{r}\left[1-\exp\left(-\dfrac{1}{4}Vr^2\right)\right]; \quad z=l \quad \text{(tangential injection at entry)}. \end{cases} \tag{39}$$

Equation (39) represents a *laminar* representation of the swirl velocity in a simulated bidirectional vortex chamber. In considering injection conditions leading to *turbulence*, one may follow Faler and Leibovich[36] or Escudier *et al.*[37] and introduce an empirically based eddy viscosity ratio ℓ_t. Being a measure of the magnification of molecular viscosity μ due to turbulence, one sets $\ell_t=\mu_t/\mu$, with μ_t denoting the turbulent viscosity. In this vein, Eq. (25) may be corrected by writing

$$V = \frac{\rho U A_i}{\mu_t L} = \frac{\rho U A_i}{\mu \ell_t L} = \frac{V_t}{\ell_t}. \tag{40}$$

The turbulent Reynolds number V_t calculated using an average laminar, molecular viscosity may hence be modified before insertion into Eq. (39). To estimate ℓ_t, the method of least-squares may be systematically applied as performed recently by Vatistas[38] in a problem involving a rotating vortex. Based on nearly 900 experimental points acquired at different vortex Reynolds numbers by Rom[39] and Anderson *et al.*[40] one finds, to good approximation, $\ell_t \simeq 152$ (see Maicke and Majdalani[41]). This empirical correction enables us to extend the range of validity for Eq. (39).

IV. RESULTS AND DISCUSSION

A. Tangential velocity

As shown in Fig. 3, the tangential component of the velocity starts from zero at the wall and then increases rapidly to merge with the outer flowfield within a characteristic distance δ_w. It continues to increase until a peak value is reached that delimits the envelope inside of which viscous forces dominate. After passing through this maximum $(u_\theta)_{\max}$, the swirl velocity then gradually depreciates within a radius δ_c until it reaches zero at the centerline. Assuming laminar conditions, a plot of u_θ in Fig. 3 is given at three vortex Reynolds numbers of 10^2, 10^3, and 10^4. Note that increasing the chamber aspect ratio is paramount to magnifying the role of viscosity according to Eq. (25).

In Fig. 3(a) and its inset, we illustrate the expansion of the radius of the core vortex δ_c with upward growth in viscosity. Here δ_c is largest at the smallest value of V. As the vortex Reynolds number is raised to 10^4, the point of maximum swirl is drawn to the core. This behavior is accompanied by an amplification in the magnitude of $(u_\theta)_{\max}$. With further increases in the vortex Reynolds number, it is clear that u_θ approaches the inviscid limit.

In the close proximity of the sidewall, Fig. 3(b) illustrates the rapid damping that the swirl velocity undergoes.

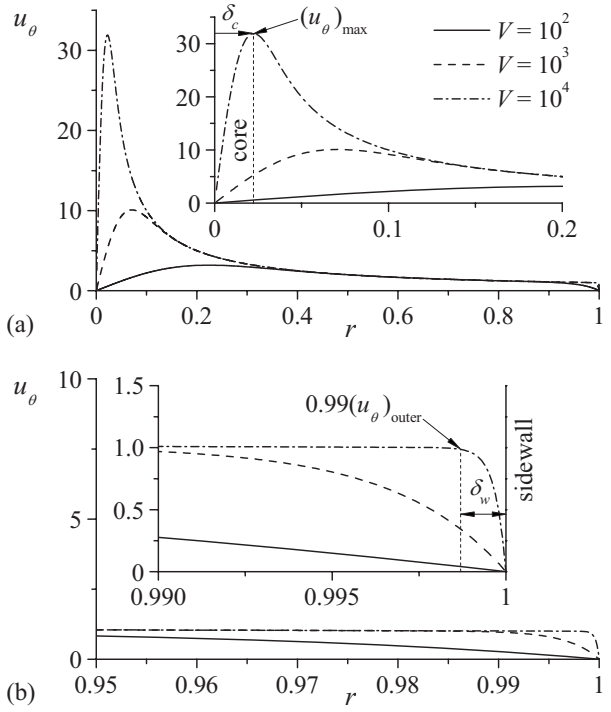

FIG. 3. Swirl velocity vs $V=\bar{Q}_i/(\nu L)$ illustrating the sensitivity of the boundary layer thickness near (a) the core and (b) the sidewall.

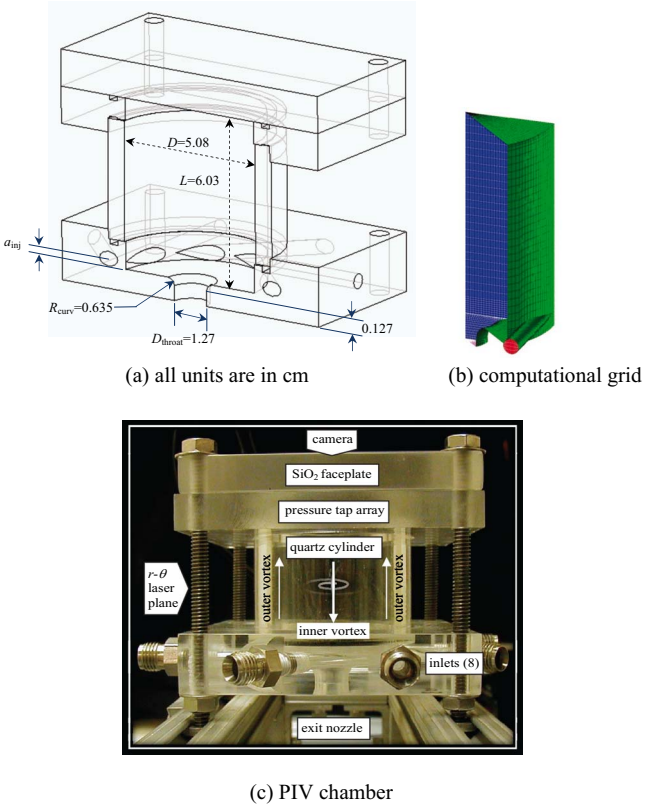

FIG. 5. (Color online) Simulated vortex engine consisting of (a) chamber assembly, (b) computational grid used by Murray *et al.* (Ref. 22) and (c) corresponding PIV chamber used by Rom *et al.* (Ref. 23).

The wall tangential boundary layer δ_w exhibits a similar dependence on viscosity. Its thickness increases when the vortex Reynolds number is decreased. The rapidly decaying curves appear to be in qualitative agreement with experimental measurements acquired by Hu *et al.*[18] They also agree with both CFD and LDV predictions obtained by Hoekstra *et al.*[17] A two-dimensional vector plot of the swirl velocity is shown in Fig. 4 with and without viscous corrections. Note that the sidewall boundary layer is thinner than the core layer depicted in Fig. 4(a).

In the interest of validating the profile predicted by Eq. (39), we seek comparisons with numerical simulations and experimental measurements obtained, respectively, from Murray *et al.*[22] and Rom *et al.*[23] The numerical runs are generated from a three-dimensional, finite-volume solver that can handle multiphase, multicomponent, chemically reacting flows. The code is based on a staggered, ALE technique that solves the integral form of the conservation equations. As such, any variation of a dependent variable within a specific control volume is correlated with the sum of the surface fluxes. The cells are mainly hexahedrons and the spatial differencing is conservative. The integral form of the equations relies on the divergence theorem to transform triple volume integrals into surface summations. In addition, the code is capable of embedding obstacle cells within the solution domain. This permits the user to introduce grids that effectively capture the presence of sharp corners without severely distorting the mesh. The model used is thoroughly tested to ensure that results are reasonably grid independent as well as time-step independent. In Fig. 5 the simulated vortex chamber assembly and computational grid are shown. Note that a 22.5° periodic boundary condition is used to exploit the pres-

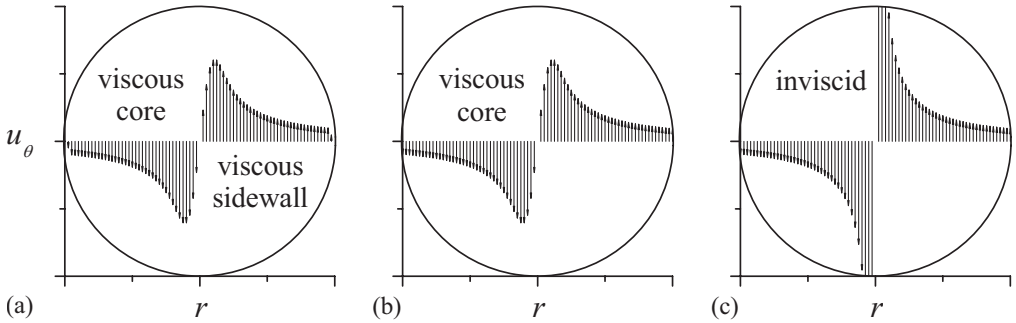

FIG. 4. Qualitative vector plot of the swirl velocity using (a) the viscous composite $u_\theta^{(c)}$, (b) composite inner $u_\theta^{(ci)}$, and (c) inviscid outer $u_\theta^{(o)}$ solutions.

TABLE I. Physical parameters for two representative vortex chamber configurations.

Parameter	Case (a)	Case (b)
Number of injector ports	8	8
Chamber pressure, $\bar{p}_0$ (kPa)	276	276
Injector pressure drop, $\Delta\bar{p}$ (kPa)	55.2 $(0.2\bar{p}_0)$	27.6 $(0.1\bar{p}_0)$
Chamber length, L (m)	0.060 325	0.060 325
Chamber radius, a (m)	0.0254	0.0254
Chamber aspect ratio, l	2.375	2.375
Injector radius, a_{inj} (m)	2.591×10^{-3}	3.048×10^{-3}
Total injection area, A_i (m^2)	1.57×10^{-4}	2.30×10^{-4}
Density, ρ (kg m^{-3})	3.183	3.183
Dynamic viscosity, μ (N s m^{-2})	1.768×10^{-5}	1.768×10^{-5}
Average injection speed, U (m s^{-1})	77.72	68.73
Modified swirl number, $\sigma=a^2/A_i$	4.10	2.81
Inflow parameter, $\kappa=A_i/(2\pi aL)$	0.0164	0.0239
Vortex Reynolds number, $V_i=\rho UA_i/(\mu L)$	36 540	47 150

ence of eight axisymmetric injectors at the base of the cylindrical chamber. Nearly 200 000 cells are used in the simulation.

The test measurements are acquired through PIV and an experimental apparatus that is elaborately described by Rom[39] and Anderson *et al.*[40] In representing the vortex chamber wall, a 360° quartz cylinder is securely clamped between two adjustable faceplates. Seeding is then provided by means of a Corona smoke generator that produces average particle sizes of 0.2 μm. To capture the motion of swirling particles, a laser beam is used to illuminate a planar sheet at right angles to the z-axis. For the purpose of comparison, two specific test cases are used corresponding to injectors with 27.6 and 55.2 kPa pressure drops. These correspond to 10% and 20% of the chamber pressure. As shown in Fig. 5(a), the chamber has an inner diameter of 5.1 cm and a length of 6.0 cm. The base of the chamber is retrofitted with a simple convergent nozzle with a throat diameter of 1.27 cm and an inlet radius of curvature of 0.635 cm. Other parameters are posted in Table I. Results from the two configurations are showcased in Fig. 6.

In both parts of Fig. 6, numerical and analytical predictions show favorable agreement at the estimated vortex Reynolds numbers; these are corroborated by the available experimental measurements, especially in the outer and sidewall regions. Four additional experimental cases are compared to the analytical solution in Fig. 7. It may be interesting to note the ability of the laminar core model with a turbulent eddy viscosity to duplicate the essential features of the flow. This behavior is consistent with the results of several experimental studies in which vortices are shown to exhibit an approximately constant angular velocity core with low turbulence levels to the extent of appearing as nearly laminar. With turbulent diffusion being restricted to an annular region about the laminar core, it is not surprising to see that the free vortex approximation in the outer domain continues to hold.

As the core is approached in Fig. 6, the experimental

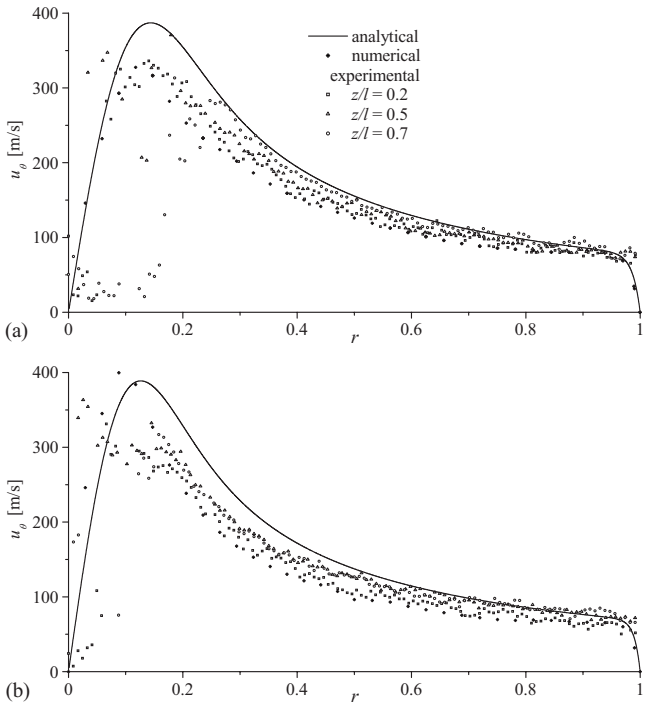

FIG. 6. Analytical swirl velocity $u_\theta^{(c)}$ vs computational and experimental predictions from Murray *et al.* (Ref. 22) and Rom *et al.* (Ref. 23). Solutions are shown at two turbulent vortex Reynolds numbers corresponding to (a) 36 540 and (b) 47 150. The experimental measurements are obtained at three different heights in the chamber corresponding to $z/l=0.2$, 0.5, and 0.7.

velocities deviate from the theoretical values projected by computations and asymptotics. The reduced fidelity of the PIV technique in the vicinity of the forced vortex region is typical and may be attributed to the intensification of viscous drag on seeded particles (see also Fig. 7). Similar trends are displayed in the RSM data and LDV measurements acquired by Hu *et al.*[18] Their LDV data acquisition system also deteriorates rapidly within the core. Several arguments could be offered as plausible explanations. While approaching $r=\delta_c$ from the outer region, particle drag increases, and the swirl velocity climbs significantly relative to the radial velocity; it becomes difficult for the particles to faithfully follow the flow or for the experimenter to achieve good seeding concentrations. In the correlated measurements reported by Rom *et al.*,[23] PIV data sets obtained with confidence are limited to $r>\delta_c$. Inside the core radius, the increased axial velocity perpendicular to the laser sheet adversely affects accurate data gathering. Due to fast axial motion near $r\to0$, particles swirling in the illuminated laser plane when a first image is taken are quickly transported outside the laser sheet before a second image can be acquired. Vortex precession and low seeding densities in the core region only exacerbate this problem, thus amplifying the observed statistical scatter. To increase the precision of measurements, it is essential to use correlated particle pairs from two pulsed laser planes. A more elaborate, two-component LDV system is hence needed to reduce the noise that accompanies the detection of highly swirling particles.

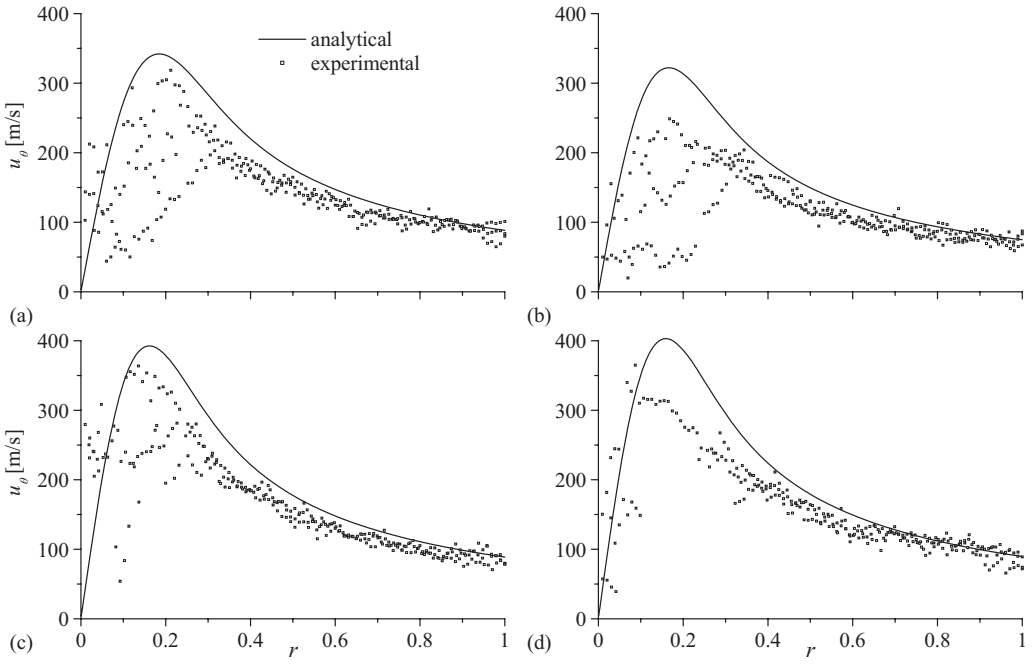

FIG. 7. Analytical swirl velocity $u_\theta^{(c)}$ vs experimental predictions from Rom *et al.* (Ref. 23). Using the same setup as before, solutions are shown at four turbulent vortex Reynolds numbers corresponding to (a) 22 370, (b) 27 650, (c) 29 150, and (d) 30 160.

B. Viscous core thickness

In order to quantify the forced vortex region, it is helpful to select a characteristic lengthscale that is commensurate with the size of the rigid-body flow region in which viscous forces are appreciable. For this purpose, we choose the radial distance from the centerline to the peak velocity $(u_\theta)_{\max}$ as our characteristic length δ_c. As shown in the inset of Fig. 3, this distance extends from the chamber axis to the center of the overlap region where the outer and inner core solutions merge. With the core region being confined to $0 \le r \le \delta_c$, we define the diameter of the forced vortex to be twice this distance.

To make headway, we recall that $\delta_c = r_{\max}$ where $r_{\max}$ is the appropriate zero of the radial derivative of u_θ. To find this root explicitly, we differentiate Eq. (39) or, equivalently, Eq. (27). We choose the latter and write

$$\frac{du_\theta^{(ci)}}{dr} = \left.\frac{(Vr^2+2)\exp\left(-\frac{1}{4}Vr^2\right)-2}{2r^2\left[1-\exp\left(-\frac{1}{4}V\right)\right]}\right|_{r=r_{\max}} = 0. \tag{41}$$

This transcendental relation yields

$$\delta_c = r_{\max} = \sqrt{2\left\{-1-2\,\mathrm{pln}\left[-1,-\tfrac{1}{2}\exp\left(-\tfrac{1}{2}\right)\right]\right\}/V} \simeq 2.2418/V^{1/2}, \tag{42}$$

where $\mathrm{pln}(x,y)$ represents the product-log function. Interestingly, the diameter of the forced vortex is expressible by $D_c = 4.4836/\sqrt{V}$. Accordingly, the thickness of the viscous core is inversely proportional to the square root of the vortex Reynolds number. This result is typical of boundary layers in steady, nonswirling flows.

A plot of δ_c versus V is given in Fig. 8. The curve also represents the locus of the maximum swirl velocity. Its invariance with the axial coordinate may be connected to the neglect of Ekman-type layers forming at the headwall. The weak sensitivity to the axial distance is corroborated, in part, by the numerical and experimental data found in the literature.

Equation (42) permits calculating the maximum swirl velocity for an arbitrary inlet area ratio, chamber aspect ratio, swirl number, and mean flow Re. Through backward substitution into Eq. (27), we retrieve

$$(u_\theta)_{\max} = \frac{\left(1-\exp\left\{\frac{1}{2}+\mathrm{pln}\left[-1,-\frac{1}{2}\exp\left(-\frac{1}{2}\right)\right]\right\}\right)\sqrt{V}}{\left[1-\exp\left(-\frac{1}{4}V\right)\right]\sqrt{\left\{-1-2\,\mathrm{pln}\left[-1,-\frac{1}{2}\exp\left(-\frac{1}{2}\right)\right]\right\}}} \simeq 0.3191V^{1/2} \tag{43}$$

As shown in Fig. 9, $(u_\theta)_{\max}$ grows with successive increases in the vortex Reynolds number. This is due to the driving speed at entry being (i) entirely tangential and (ii) directly proportional to the vortex Reynolds number. For an experimental range of $10^4 \le V_t \le 10^5$, the modified vortex

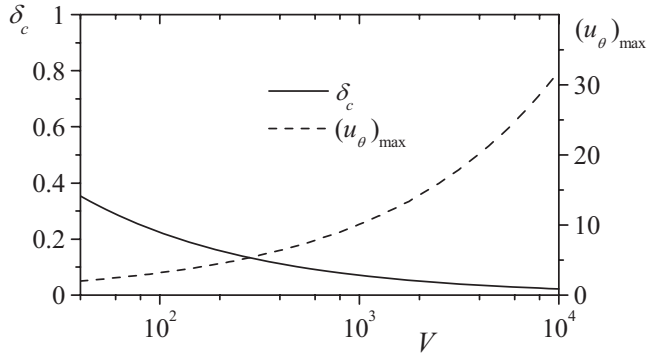

FIG. 8. Variation of the core layer thickness (left scale) and maximum tangential speed (right) with respect to the vortex Reynolds number.

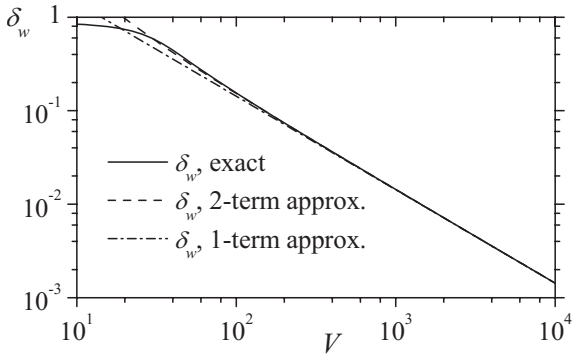

FIG. 9. Variation of the wall tangential boundary layer thickness with respect to the vortex Reynolds number. The two-term expression is valid for $V>107$ with a less than 1% error.

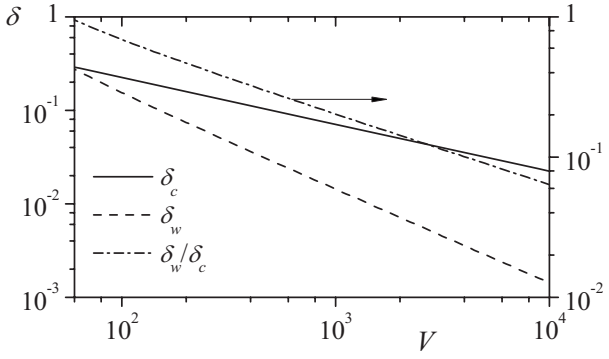

FIG. 10. Relative sizes of inner core and sidewall boundary layers.

Reynolds number varies between 66 and 660. The corresponding δ_c decreases from 27.5% to 8.7% while the maximum velocity is computed to be 2.6–8.2 times larger than the average injection speed. The presence of high tangential velocities is, indeed, reported in some experiments.[23,40]

C. Wall tangential layer thickness

The size of the sidewall boundary layer may be quantified by defining δ_w to be the distance from the wall to the point where the tangential velocity reaches 99% of its final, outer value. To find this point, we set $u_\theta^{(c)}=0.99u_\theta^{(o)}$. Being in the close proximity of the wall, this condition translates into $u_\theta^{(w)}=0.99u_\theta^{(o)}$, where $u_\theta^{(w)}$ is given by Eq. (37). Imposing this constraint on $u_\theta^{(w)}$ instead of $u_\theta^{(c)}$ is necessary lest an explicitly noninvertible problem is obtained. Letting r_w be the radius at which wall effects become negligible, one solves

$$\frac{1}{r_w}\left\{\frac{1-\exp\left[-\frac{1}{4}\alpha V(1-r_w^2)\right]}{1-\exp\left(-\frac{1}{4}\alpha V\right)}\right\}=\left(1-\frac{1}{100}\right)\frac{1}{r_w}, \tag{44}$$

$$\alpha\equiv\tfrac{1}{6}\pi^2-1\simeq 0.644\,934$$

to get

$$\delta_w=1-r_w=1-\sqrt{1+\frac{4\ln\left[0.01+0.99\exp\left(-\frac{1}{4}\alpha V\right)\right]}{\alpha V}}$$

$$\simeq 1-\sqrt{1-\frac{28.5621}{V}}. \tag{45}$$

The wall approximation is valid for $V>49$. Furthermore, an expansion of the radical may be attempted to obtain

$$\delta_w=\frac{4\ln 10}{\alpha V}\left[1+2\left(\frac{\ln 10}{\alpha V}\right)+8\left(\frac{\ln 10}{\alpha V}\right)^2+\cdots\right]$$

$$\simeq\frac{14.281}{V}\left(1+\frac{7.1405}{V}+\cdots\right). \tag{46}$$

Bearing a relative error of less than 1% for $V>722$, a one-term approximation, $\delta_w\simeq 14.281/V$, may be used for sufficiently large V. The foregoing expressions are compared in Fig. 9 to confirm that the wall tangential boundary layer is inversely proportional to the vortex Reynolds number. This explains the reduced thickness relative to the core layer. To further illustrate this point, both δ_w and δ_c are compared on a log-log scale in Fig. 10. In addition to the clear asymptotic slopes of order one and one-half, respectively, the graph displays the wall-to-core ratio. This ratio decreases by nearly one order of magnitude, from 0.69 to 0.064, as the vortex Reynolds number is increased from 10^2 to 10^4. Note that the wall-to-core ratio is represented by the chained line in Fig. 10. It may be estimated from

$$\frac{\delta_w}{\delta_c}\simeq 0.446\,068\sqrt{V}\left(1-\sqrt{1-\frac{28.5621}{V}}\right)$$

$$\simeq\frac{6.3703}{\sqrt{V}}\left(1+\frac{7.1405}{V}+\cdots\right);\quad V>49. \tag{47}$$

D. Vorticity correction

The region corresponding to $0\le r\le\delta_c$ denotes the viscous core flanked circumferentially by an outer field that is predominantly inviscid. We find that flow rotationality in the outer region is slightly altered due to viscous interactions with the forced vortex. An assessment of vorticity leads to

$$\mathbf{\Omega}=4\pi^2\kappa rz\sin(\pi r^2)\mathbf{e}_\theta$$

$$+\frac{V}{2}\left\{\frac{\exp\left(-\frac{1}{4}Vr^2\right)}{1-\exp\left(-\frac{1}{4}V\right)}-\frac{\alpha\exp\left[-\frac{1}{4}\alpha V(1-r^2)\right]}{1-\exp\left(-\frac{1}{4}\alpha V\right)}\right\}\mathbf{e}_z. \tag{48}$$

It may be helpful to note that, as $\varepsilon\to 0$, the vorticity of the inviscid solution is restored.[29] The viscous-induced Ω_z may be calculated from

$$\Omega_z\simeq\tfrac{1}{2}V\left\{\exp\left(-\tfrac{1}{4}Vr^2\right)-\alpha\exp\left[-\tfrac{1}{4}\alpha V(1-r^2)\right]\right\}. \tag{49}$$

This term is important near $z=0$, where the azimuthal component of the vorticity vanishes. The same occurs near the centerline. Overall, we find that the sidewall boundary layer correction reduces the variability of the vorticity with the axial distance.

In reference to Eq. (28), the near-core motion is

prescribed by a linear relation between the swirl velocity and the radial coordinate as $r \to 0$. Being of the form $u_\theta = \omega_f r$, the angular speed of the forced vortex can be estimated from Eq. (29). Accordingly, so long as $V > 10$, one can take $\omega_f = \frac{1}{4}V$. This simple outcome represents the characteristic angular speed of the rotating core layer.

E. Pressure behavior

In view of the viscous corrections affecting the tangential velocity, an assessment of the radial component of the pressure gradient is necessary. Starting with Euler's equation, one finds

$$\frac{\partial p}{\partial r} \simeq r^{-3}\left\{1 - \exp\left(-\tfrac{1}{4}Vr^2\right) - \exp\left[-\tfrac{1}{4}\left(\tfrac{1}{6}\pi^2 - 1\right)V(1-r^2)\right]\right\}^2 + \kappa^2 r^{-3}\sin(\pi r^2)[\sin(2\pi r^2) - 2\pi r^2\cos(2\pi r^2)]. \tag{50}$$

The axial pressure gradient is simpler as it collapses into a single expression that is independent of r:

$$\frac{\partial p}{\partial z} = -4\pi^2\kappa^2 z. \tag{51}$$

Partial integration is straightforward because Eqs. (50) and (51) are independent of z and r, respectively. The spatial distribution of the pressure becomes

$$\begin{aligned} p = p_0 &- 2\pi^2\kappa^2 z^2 - \tfrac{1}{2}r^{-2}\left(\left[1 - \exp\left(-\tfrac{1}{4}Vr^2\right)\right]^2 + \left\{1 - \exp\left[-\tfrac{1}{4}\alpha V(1-r^2)\right]\right\}^2 - 1 + \kappa^2\sin^2(\pi r^2)\right) \\ &+ \tfrac{1}{4}V\left[\mathrm{Ei}\left(-\tfrac{1}{4}Vr^2\right) - \mathrm{Ei}\left(-\tfrac{1}{2}Vr^2\right) + \alpha\exp\left(-\tfrac{1}{2}\alpha V\right)\mathrm{Ei}\left(\tfrac{1}{2}\alpha Vr^2\right) - \alpha\exp\left(-\tfrac{1}{4}\alpha V\right)\mathrm{Ei}\left(\tfrac{1}{4}\alpha Vr^2\right)\right] \\ &- \tfrac{1}{4}\alpha V\exp\left(-\tfrac{1}{4}\alpha V\right)\left[\exp\left(-\tfrac{1}{4}\alpha V\right)\mathrm{Ei}\left(\tfrac{1}{2}\alpha V\right) - \mathrm{Ei}\left(\tfrac{1}{4}\alpha V\right)\right], \end{aligned} \tag{52}$$

where $\mathrm{Ei}(x)$ refers to the second exponential integral function given by[42]

$$\mathrm{Ei}(x) = \gamma + \ln|x| + \sum_{m=1}^{\infty}\frac{x^m}{m!\,m}, \tag{53}$$

$$\gamma \simeq 0.577\ 215\ 664\ 9 \quad (\text{Euler's constant}).$$

Note that p_0 is a reference pressure that depends on operating conditions. Ordinarily, one would consider the suitability of the pressure at the origin, (0,0). However, based on experimental observations and numerical simulations, more confidence in the data is achieved at $r = 1$.[17,18] Near the core, not only is a visible scatter in the data frequently reported, but the centerline values also become sensitive to the model in question.[22,23] In the bidirectional vortex, another factor is relevant. The pressure at the sidewall is the largest due to the role played by centrifugal forces. Near the centerline, a suction effect is created. It is therefore more convenient to take the maximum pressure in the chamber, $p_0 = p(1,0)$, as the reference pressure. This choice helps to normalize the pressure data, p/p_0, on a [0,1] interval.

As far as viscosity is concerned, it is apparent that its inclusion in the tangential momentum balance has an appreciable impact not only on the pressure distribution but also on the swirl velocity, mean flow vorticity, and radial pressure gradient. This behavior is illustrated next.

The pressure distribution and its radial gradient are displayed at the headwall in Fig. 11. From this graph, one infers that the pressure drop increases in the radial direction due to the effect of centrifugal forces. Moreover, the pressure distribution in the axial direction seems negligible when compared to the rapid radial variations. With the advent of viscous corrections, the pressure gradient in Fig. 11(a) passes through a maximum as one approaches the core. This peak may be calculated from Eq. (50). Further, the pressure peak

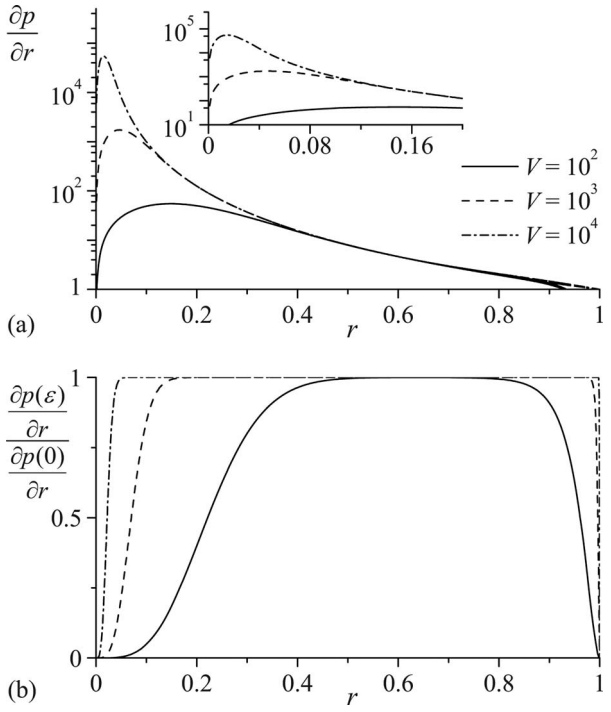

FIG. 11. Radial variation at select values of V and l for (a) the pressure gradient and (b) the pressure gradient referenced to its inviscid value.

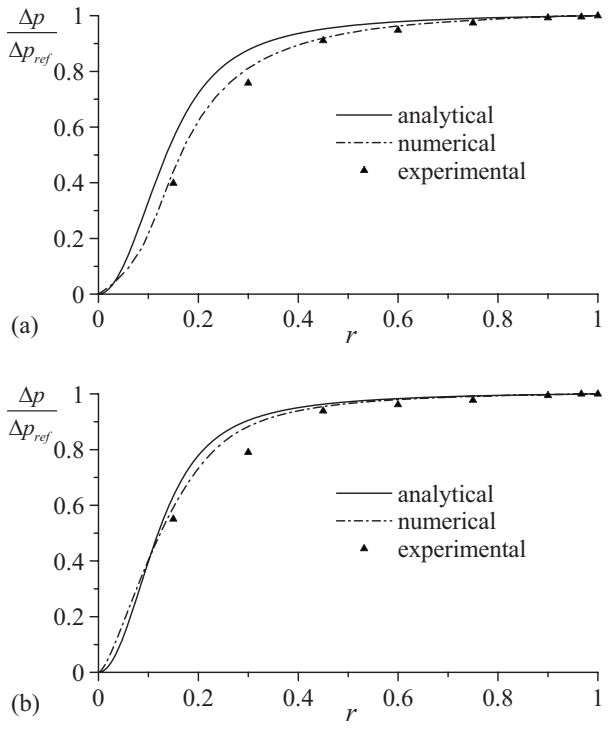

FIG. 12. Asymptotic, numerical, and experimental results acquired at the headwall for cases (a) $V_t=36\,540$, $\kappa=0.016$, and (b) $V_t=47\,150$, $\kappa=0.024$. Experimental results are obtained by Chiaverini at eight radial locations; CFD results are by Murray *et al.* (Ref. 22).

shown in Fig. 11(a) increases in magnitude and moves closer to the axis of the chamber when V is raised. This behavior is consistent with a forced vortex.

When the radial pressure gradient is normalized by its inviscid value as in Fig. 11(b), it becomes virtually independent of l or σ due to the small influence of κ^2; however, it remains a strong function of V. The same can be said of the pressure shown in Fig. 12.

The actual pressure is normalized by its maximum radial value $p_0=p(1,0)$ taken at the headwall. Results are shown in Fig. 12 side-by-side with numerical simulations obtained by Murray *et al.*[22] The case for comparison corresponds to that of Fig. 6(a). The simulated runs are plotted at three different times. These show the same trends, especially in the outer and wall regions. All numerical curves converge to the same value at the sidewall. However, as the vortex core is approached, deviations in the data start to appear. At the centerline, a minor scatter is observed. This scatter may be attributed to the increased resolution requirements on the numerical code in the forced vortex region. A similar pressure behavior is reported by Hu *et al.*[18] or Hoekstra *et al.*[17]

Based on Eq. (50), one can calculate the radial distance δ_p corresponding to the point of maximum $\partial p/\partial r$. Starting with

$$\left.\frac{d}{dr}\left(\frac{\partial p}{\partial r}\right)\right|_{r_{\max}}=0, \tag{54}$$

an asymptotic expression for $\delta_p=r_{\max}$ is obtained, specifically,

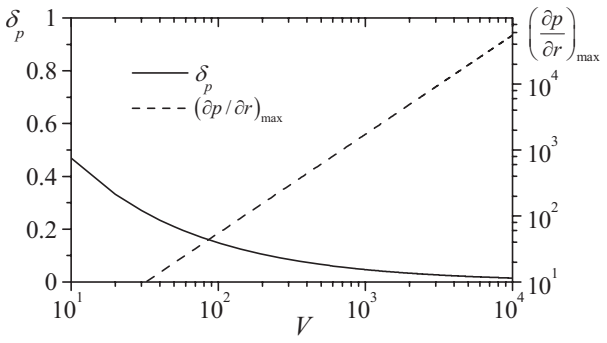

FIG. 13. Maximum radial pressure gradient and its locus vs V.

$$\delta_p \simeq 1.4835/V^{1/2}. \tag{55}$$

Given $V\geq 100$, the relative error associated with Eq. (55) is negligible, being less than 0.037% for $\sigma\geq 1$ and less than 3.5×10^{-5}% for $\sigma\geq 25$. This error drops precipitously with successive increases in V or σ. Note that the maximum radial pressure gradient is closer to the core than the maximum swirl velocity. This is due to

$$\delta_p/\delta_c \simeq 0.662. \tag{56}$$

In view of $\delta_p\sim\delta_c\sim V^{-1/2}$, the thickness of the core shown in Fig. 13 is confirmed to be inversely proportional to $V^{1/2}$. Having determined δ_p, the corresponding pressure gradient may be evaluated from

$$\left.\frac{\partial p}{\partial r}\right|_{\max}=\frac{0.054\,846\,6V^{3/2}}{\left[1-\exp\left(-\frac{1}{2}V\right)\right]^2}\simeq 0.054\,846\,6V^{3/2}. \tag{57}$$

As before, the relative error in Eq. (57) is negligible, namely, below 0.14% for $\sigma\geq 1$ and below 0.07% for $\sigma\geq 25$. Note that the maximum radial pressure gradient is plotted on the right-hand-side of Fig. 13.

F. Wall stress tensor

The shear stresses may be calculated from

$$\tau_{rr}=2\varepsilon\frac{\partial u_r}{\partial r}=\varepsilon^2 V\left[\frac{\sin(\pi r^2)}{\pi r^2}-2\cos(\pi r^2)\right], \tag{58}$$

$$\tau_{\theta\theta}=2\varepsilon\left(\frac{1}{r}\frac{\partial u_\theta}{\partial\theta}+\frac{u_r}{r}\right)=2\varepsilon\frac{u_r}{r}=-\varepsilon^2 V\frac{\sin(\pi r^2)}{\pi r^2}, \tag{59}$$

$$\tau_{zz}=2\varepsilon\frac{\partial u_z}{\partial z}=2\varepsilon^2 V\cos(\pi r^2), \tag{60}$$

$$\tau_{r\theta} = \varepsilon r \frac{\partial}{\partial r}\left(\frac{u_\theta}{r}\right)$$
$$= \frac{\varepsilon}{r^2}\left\{\frac{\exp\left(-\frac{1}{4}Vr^2\right)\left(2+\frac{1}{2}Vr^2\right)}{1-\exp\left(-\frac{1}{4}V\right)} + \frac{\exp\left[-\frac{1}{4}\alpha V(1-r^2)\right]\left(2-\frac{1}{2}\alpha Vr^2\right)-1-\exp\left(-\frac{1}{4}\alpha V\right)}{1-\exp\left(-\frac{1}{4}\alpha V\right)} - \coth\left(\frac{V}{8}\right)\right\}$$
$$\simeq \frac{\varepsilon}{r^2}\left\{\exp\left(-\tfrac{1}{4}Vr^2\right)\left(2+\tfrac{1}{2}Vr^2\right) + \exp\left[-\tfrac{1}{4}\alpha V(1-r^2)\right]\left(2-\tfrac{1}{2}\alpha Vr^2\right)-2\right\}, \quad (61)$$

$$\tau_{\theta z} = \varepsilon\left(\frac{1}{r}\frac{\partial u_z}{\partial \theta} + \frac{\partial u_\theta}{\partial z}\right) = 0, \quad (62)$$

$$\tau_{zr} = \varepsilon\left(\frac{\partial u_z}{\partial r} + \frac{\partial u_r}{\partial z}\right) = \varepsilon\frac{\partial u_z}{\partial r} = -2\pi\varepsilon^2 Vrz\sin(\pi r^2). \quad (63)$$

It is clear that the resultant is dominated by the tangential shear stress, $\tau_{r\theta}$. At the wall, these quantities become

$$\tau_{rr}^{(w)} = 2\varepsilon^2 V, \quad \tau_{\theta\theta}^{(w)} = 0, \quad \tau_{zz}^{(w)} = -2\varepsilon^2 V,$$
$$\tau_{r\theta}^{(w)} = -\tfrac{1}{2}\alpha\varepsilon V = -\pi\alpha\kappa, \quad \tau_{\theta z}^{(w)} = 0, \quad \tau_{zr}^{(w)} = 0. \quad (64)$$

The total shear stress is hence $\tau_0^{(w)} = -\frac{1}{2}\alpha\varepsilon V\sqrt{1+32\varepsilon^2/\alpha^2} \simeq -\frac{1}{2}\alpha\varepsilon V = -\pi\left(\frac{1}{6}\pi^2-1\right)\kappa = -2.026\kappa$. Contributions due to $\tau_{rr}^{(w)}$ and $\tau_{zz}^{(w)}$ are negligible, being of $O(\varepsilon^2)$.

G. Swirling intensity

The swirling intensity defined by Chang and Dhir[43] may be evaluated for the present model. In the context of a bidirectional vortex, we recover

$$\tilde{\Omega} = \frac{1}{4}\left(\int_0^{1/\sqrt{2}} u_z r dr\right)^{-2}\int_0^{1/\sqrt{2}} u_z u_\theta r dr. \quad (65)$$

Using symbolic programming, Eq. (65) may be integrated, rearranged, and simplified into

$$\tilde{\Omega} = -\frac{\pi\sqrt{\pi}(1-i)}{4\sqrt{2}}\frac{1}{\kappa z}\left\{\frac{\mathrm{erf}\left[\frac{1}{4}(1+i)\sqrt{4\pi-iV}\right]}{\sqrt{4\pi-iV}} + \frac{\mathrm{erfi}\left[\frac{1}{4}(1+i)\sqrt{4\pi+iV}\right]}{\sqrt{4\pi+iV}} - \frac{(1+i)}{\sqrt{\pi}}C(1)\right\}, \quad (66)$$

where transcendentally small terms are ignored. Here $i = \sqrt{-1}$, $C(1) \simeq 0.779\,893$ and $C(x)$ is the Fresnel integral,

$$C(x) = \int_0^x \cos\left(\frac{1}{2}\pi r^2\right)dr$$
$$= x - \frac{1}{40}\pi^2 x^5 + \frac{1}{3456}\pi^4 x^9 + O(x^{13}). \quad (67)$$

Using suitable asymptotic expansions for $V \gg 1$, the complexity of Eq. (66) may be reduced by expressing it as a three-term series approximation,

$$\tilde{\Omega} = \frac{1}{\kappa z}\left[\frac{\sqrt{2}\pi C(1)}{4} - \frac{\pi^{3/2}}{2V^{1/2}} + \frac{3\pi^{7/2}}{V^{5/2}} + O(V^{-9/2})\right]$$
$$\simeq \frac{0.866\,244 - 2.784\,16V^{-1/2} + 164.872V^{-5/2}}{\kappa z}. \quad (68)$$

To illustrate the dependence of the swirling intensity on the vortex Reynolds number, the product of the inflow parameter, axial coordinate, and swirling intensity $\kappa z\tilde{\Omega}$ is plotted in Fig. 14 as a function of V. This group parameter is shown to vary between 0.2 and 0.8662. Due to the rapid convergence of the series in Eq. (68), it seems that a two-term approximation is adequate for $V \geq 60$. Note that $\tilde{\Omega}$ is largest near the headwall and increases at higher vortex Reynolds numbers. Its behavior is particularly favorable to applications that are poised to profit from higher rates of mixing and turbulence. One may cite the bidirectional vortex engine as one such example because of its fuel injection being located directly beneath the headwall.[44] In closing, we post in Table II the key variables and parameters connected to the complex lamellar, viscous bidirectional vortex. This table includes the small viscous corrections needed to satisfy the no slip condition in both axial and radial directions. Their asymptotic derivation mirrors the tangential velocity analysis presented here and is provided in detail by Batterson and Majdalani.[45]

V. CONCLUSIONS

In this study, a viscous solution is obtained for a complex lamellar form of the bidirectional vortex arising in a simulated, swirl-dominated, thrust chamber. The viscous corrections we derive suppress the unbounded behavior of the

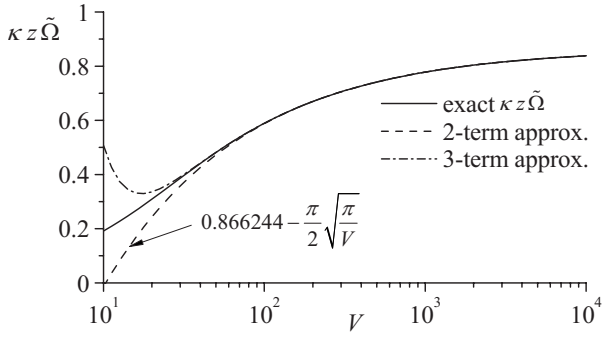

FIG. 14. Swirling intensity product, $\kappa z\tilde{\Omega}$.

TABLE II. Characteristic variables and parameters for the complex lamellar form of the bidirectional vortex.

Name	Parameter	Value
Radial velocity	u_r	$-\kappa\frac{\sin(\pi r^2)}{r}\left\{1-\exp\left[-\frac{1}{4}\left(\frac{1}{6}\pi^2-1\right)V(1-r^2)\right]\right\}$
Swirl velocity	u_θ	$\begin{cases}\frac{1}{r}\left\{1-\exp\left(-\frac{1}{4}Vr^2\right)-\exp\left[-\frac{1}{4}\left(\frac{1}{6}\pi^2-1\right)V(1-r^2)\right]\right\}; & 0<z<l\\ \frac{1}{r}\left[1-\exp\left(-\frac{1}{4}Vr^2\right)\right]; & z=l \quad \text{(tangential injection at entry)}\end{cases}$
Axial velocity	u_z	$2\pi\kappa z\cos(\pi r^2)\left\{1-\exp\left[-\frac{1}{4}\left(\frac{1}{6}\pi^2-1\right)V(1-r^2)\right]\right\}$
Vorticity	$\mathbf{\Omega}$	$4\pi^2\kappa r z\sin(\pi r^2)\mathbf{e}_\theta+\frac{1}{2}V\left\{\exp\left(-\frac{1}{4}Vr^2\right)-\alpha\exp\left[-\frac{1}{4}\alpha V(1-r^2)\right]\right\}\mathbf{e}_z$
Radial pressure gradient	$\frac{\partial p}{\partial r}$	$r^{-3}\left\{1-\exp\left(-\frac{1}{4}Vr^2\right)-\exp\left[-\frac{1}{4}\left(\frac{1}{6}\pi^2-1\right)V(1-r^2)\right]\right\}^2$ $+\kappa^2 r^{-3}\sin(\pi r^2)[\sin(2\pi r^2)-2\pi r^2\cos(2\pi r^2)]$
Axial pressure gradient	$\frac{\partial p}{\partial z}$	$-4\pi^2\kappa^2 z$
Core boundary layer	δ_c	$2.2418/\sqrt{V}=2.2418/\sqrt{V_t/\ell_t}$
Maximum swirl	$(u_\theta)_{\max}$	$0.3191\sqrt{V}=0.3191\sqrt{V_t/\ell_t}$
Wall boundary layer	δ_w	$1-\sqrt{1-28.56/V}\simeq 14.28(1+7.14/V)/V$
Core angular rotation	ω_f	$\frac{1}{4}V$
Swirling intensity	$\tilde{\Omega}$	$(0.866\,244-2.784\,16V^{-1/2}+164.872V^{-5/2})/\kappa z$
Inflow parameter	κ	$\frac{1}{2\pi\sigma l}=\frac{\bar{Q}_i}{2\pi UaL}=\frac{A_i}{2\pi aL}$
Modified swirl number	σ	$\frac{\sqrt{2}}{\pi}S=\frac{Ua^2}{\bar{Q}_i}=\frac{a^2}{A_i}$
Vortex Reynolds number	V	$\frac{1}{\varepsilon\sigma l}=\frac{\mathrm{Re}}{\sigma}\frac{a}{L}=\begin{cases}\frac{\rho UA_i}{\mu L}=\frac{\dot{m}_i}{\mu L}; & \text{(laminar)}\\ \frac{\rho UA_i}{\mu_t L}=\frac{\dot{m}_i}{\mu\ell_t L}=\frac{V_t}{\ell_t}; & \text{(turbulent)}\end{cases}$

swirl velocity and pressure distribution at the centerline. They also permit securing the velocity adherence requirement at the sidewall.

Based on the present analytical results, the thickness of the forced vortex is characterized as a function of the chamber aspect ratio, the swirl number, and the flow Reynolds number. We find that the viscous core decreases with the square root of the vortex Reynolds number, a byproduct of the mean flow Reynolds number, the swirl number, and the chamber aspect ratio. When either the kinematic viscosity or the chamber length is increased, the diameter of the forced vortex is magnified according to $\delta_c \sim V^{-1/2}$. Being proportional to $(\nu L/\bar{Q}_i)^{1/2}$, the core thickness undergoes successive expansions with upward changes in the chamber length and viscosity, or when the injected flow rate is reduced. It typically varies with $\delta_c \simeq 2.24/\sqrt{V}$.

The wall boundary layer δ_w is found to be smaller, and its relative thickness with respect to the core layer diminishes with successive increases in V. At Reynolds numbers exceeding 700, it becomes directly proportional to $\nu L/\bar{Q}_i$ and may be approximated by $\delta_w \simeq 14.28/V$.

The inclusion of viscous forces leads to rapid damping of the swirl velocity. Under some simulated turbulent conditions, the peak velocity ascends to as high as eight times the average injection speed. Our analysis tracks its rise and subsequent fall at both the centerline and sidewall. Similar trends are exhibited by the pressure and its radial gradient. Here friction is seen to engender a small nonzero axial vorticity component that vanishes as the sidewall is approached. Due to mounting friction around the chamber axis, the cylindrical core rotates as a rigid body with an average angular speed of $\omega_f = \frac{1}{4}V$. Being proportional to $\bar{Q}_i/(\nu L)$, the angular frequency of the forced vortex increases with the injection flow rate. It is also higher in shorter chambers with smaller viscosity. These results help to quantify some of the key features of bidirectional vortex motion while increasing our set of tools for the treatment of confined swirling flows. In

future work, it is hoped that the endwall boundary layers will be explored in addition to the viscous analysis of other Eulerian solutions that have been introduced in recent work.[31]

ACKNOWLEDGMENTS

This work is sponsored partly by the National Science Foundation through Grant No. CMMI-0928762 and partly by Orbital Technologies Corporation. The authors are deeply grateful for the experimental data provided by Dr. Mark H. Anderson from the University of Wisconsin.

[1] J. K. Harvey, "Some observations of the vortex breakdown phenomenon," J. Fluid Mech. **14**, 585 (1962).
[2] S. Leibovich, "The structure of vortex breakdown," Annu. Rev. Fluid Mech. **10**, 221 (1978).
[3] S. Leibovich, "Vortex stability and breakdown: Survey and extension," AIAA J. **22**, 1192 (1984).
[4] R. R. Long, "Sources and sinks at the axis of a rotating liquid," Q. J. Mech. Appl. Math. **9**, 385 (1956).
[5] J. M. Burgers, "A mathematical model illustrating the theory of turbulence," Adv. Appl. Mech. **1**, 171 (1948).
[6] C. W. Oseen, "Uber Wirbelbewegune in einer reibenden Flussigkeit," Ark. Mat., Astron. Fys. **7**, 14 (1912).
[7] G. Hamel, "Spiralformige bewegung zaher Flussigkeit," Jahresber. Dtsch. Math.-Ver. **25**, 34 (1916).
[8] H. Schlichting, *Boundary-Layer Theory*, 7th ed. (McGraw-Hill, New York, 1979).
[9] W. S. Lewellen, "A review of confined vortex flows," NASA Technical Report No. CR-1772, 1971.
[10] G. H. Vatistas, "Tangential velocity and static pressure distributions in vortex chambers," AIAA J. **25**, 1139 (1987).
[11] D. F. Kelsall, "A study of motion of solid particles in a hydraulic cyclone," Trans. Inst. Chem. Eng. **30**, 87 (1952).
[12] J. L. Smith, "An experimental study of the vortex in the cyclone separator," J. Basic Eng. **84**, 602 (1962).
[13] J. L. Smith, "An analysis of the vortex flow in the cyclone separator," J. Basic Eng. **84**, 609 (1962).
[14] R. F. Reydon and W. H. Gauvin, "Theoretical and experimental studies of confined vortex flow," Can. J. Chem. Eng. **59**, 14 (1981).
[15] G. H. Vatistas, S. Lin, and C. K. Kwok, "Theoretical and experimental studies on vortex chamber flows," AIAA J. **24**, 635 (1986).
[16] A. Ogawa, "Estimation of the collection efficiencies of the three types of the cyclone dust collectors from the standpoint of the flow pattern in the cylindrical cyclone dust collectors," Bull. JSME **27**, 64 (1984).
[17] A. J. Hoekstra, J. J. Derksen, and H. E. A. Van den Akker, "An experimental and numerical study of turbulent swirling flow in gas cyclones," Chem. Eng. Sci. **54**, 2055 (1999).
[18] L. Y. Hu, L. X. Zhou, J. Zhang, and M. X. Shi, "Studies of strongly swirling flows in the full space of a volute cyclone separator," AIChE J. **51**, 740 (2005).
[19] J. J. Derksen and H. E. A. Van den Akker, "Simulation of vortex core precession in a reverse-flow cyclone," AIChE J. **46**, 1317 (2000).
[20] D. Fang, J. Majdalani, and M. J. Chiaverini, "Simulation of the cold-wall swirl driven combustion chamber," AIAA Paper No. 2003–5055, Huntsville, AL, 2003.
[21] F. Boysan, W. H. Ayers, and J. Swithenbank, "A fundamental mathematical modelling approach to cyclone design," Am. Inst. Chem. Eng. Symp. Ser. **60**, 222 (1982).
[22] A. L. Murray, A. J. Gudgen, M. J. Chiaverini, J. A. Sauer, and W. H. Knuth, "Numerical code development for simulating gel propellant combustion processes," JANNAF Paper No. 2004-0115, Las Vegas, NV, 2004.
[23] C. J. Rom, M. H. Anderson, and M. J. Chiaverini, "Cold flow analysis of a vortex chamber engine for gelled propellant combustor applications," AIAA Paper No. 2004–3359, Fort Lauderdale, FL, 2004.
[24] G. H. Vatistas, A. M. Jawarneh, and H. Hong, "Flow characteristics in a vortex chamber," Can. J. Chem. Eng. **83**, 425 (2005).
[25] M. J. Chiaverini, M. J. Malecki, J. A. Sauer, and W. H. Knuth, "Vortex combustion chamber development for future liquid rocket engine applications," AIAA Paper No. 2002–2149, Indianapolis, IN, 2002.
[26] P. W. Gloyer, W. H. Knuth, and J. Goodman, "Overview of initial research into the effects of strong vortex flow on hybrid rocket combustion and performance," CSTAR Fifth Annual Symposium N96–16953, Tullahoma, TN, 1993.
[27] W. H. Knuth, M. J. Chiaverini, J. A. Sauer, and D. J. Gramer, "Solid-fuel regression rate behavior of vortex hybrid rocket engines," J. Propul. Power **18**, 600 (2002).
[28] I. Matveev, S. Matveeva, and S. Serbin, "Design and preliminary test results of the plasma assisted tornado combustor," AIAA Paper No. 2007–5628, Cincinnati, OH, 2007.
[29] A. B. Vyas and J. Majdalani, "Exact solution of the bidirectional vortex," AIAA J. **44**, 2208 (2006).
[30] J. Majdalani and S. W. Rienstra, "On the bidirectional vortex and other similarity solutions in spherical coordinates," Z. Angew. Math. Phys. **58**, 289 (2007).
[31] J. Majdalani, "Exact Eulerian solutions of the cylindrical bidirectional vortex," AIAA Paper No. 2009–5307, Denver, CO, 2009.
[32] S. Balachandar, J. D. Buckmaster, and M. Short, "The generation of axial vorticity in solid-propellant rocket-motor flows," J. Fluid Mech. **429**, 283 (2001).
[33] M. I. G. Bloor and D. B. Ingham, "The flow in industrial cyclones," J. Fluid Mech. **178**, 507 (1987).
[34] R. D. Sullivan, "A two-cell vortex solution of the Navier–Stokes equations," J. Aerosp. Sci. **26**, 767 (1959).
[35] A. Erdélyi, *Asymptotic Expansions* (Dover, New York, 1956).
[36] J. H. Faler and S. Leibovich, "An experimental map of the internal structure of a vortex breakdown," J. Fluid Mech. **86**, 313 (1978).
[37] M. P. Escudier, J. Bornstein, and N. Zehnder, "Observations and LDA measurements of confined turbulent vortex flow," J. Fluid Mech. **98**, 49 (1980).
[38] G. H. Vatistas, "Simple model for turbulent tip vortices," J. Aircr. **43**, 1577 (2006).
[39] C. J. Rom, "Flow field and near nozzle fuel spray characterizations for a cold flowing vortex engine," M.S. dissertation, University of Wisconsin, 2006.
[40] M. H. Anderson, R. Valenzuela, C. J. Rom, R. Bonazza, and M. J. Chiaverini, "Vortex chamber flow field characterization for gelled propellant combustor applications," AIAA Paper No. 2003–4474, Huntsville, AL, 2003.
[41] B. A. Maicke and J. Majdalani, "A constant shear stress core flow model of the bidirectional vortex," Proc. R. Soc. London, Ser. A **465**, 915 (2009).
[42] M. Abramowitz and I. A. Stegun, *Handbook of Mathematical Functions* (National Bureau of Standards, New York, 1964).
[43] F. Chang and V. K. Dhir, "Mechanisms of heat transfer enhancement and slow decay of swirl in tubes with tangential injection," Int. J. Heat Fluid Flow **16**, 78 (1995).
[44] M. J. Chiaverini, M. J. Malecki, J. A. Sauer, W. H. Knuth, and J. Majdalani, "Vortex thrust chamber testing and analysis for O2-H2 propulsion applications," AIAA Paper No. 2003–4473, Huntsville, AL, 2003.
[45] J. W. Batterson and J. Majdalani, "On the boundary layers of the bidirectional vortex," AIAA Paper No. 2007–4123, Miami, FL, 2007.